Astrocyte nanoscale morphology controls Ca^{2+} signals at tripartite synapses

Audrey DENIZOT [1*], Misa ARIZONO [2, 3], U. Valentin NÄGERL[2, 3], Hugues BERRY[4, 5], De Schutter Erik[1],

1 Okinawa Institute of Science and Technology, Computational Neuroscience Unit, Onna-Son, Japan
2 Interdisciplinary Institute for Neuroscience, Université de Bordeaux, Bordeaux, France
3 Interdisciplinary Institute for Neuroscience, CNRS UMR 5297, Bordeaux, France
4 Univ Lyon, LIRIS, UMR5205 CNRS, F-69621, Villeurbanne, France
5 INRIA, F-69603, Villeurbanne, France

* audrey.denizot3@oist.jp

Abstract

Ca^{2+} signals in astrocytes can trigger the modulation of neuronal activity. Recent developments in Ca^{2+} imaging and super-resolution microscopy have allowed to characterize the complex morphology of astrocyte branchlets that communicate with neurons and the associated Ca^{2+} microdomains. Here, we use computational tools to investigate the causal relationship between branchlet morphology and spatio-temporal profile of Ca^{2+} signals. 3D reticular branchlet geometries were designed, alternating between large (nodes) and thinner cellular compartments (shafts). Simulations confirm experimental observations that a decreased shaft width is associated with a decreased diffusion flux from nodes, enhancing local Ca^{2+} activity. Upon successive neuronal stimuli, a decreased shaft width facilitates signal propagation in astrocyte branchlets. We further identify parameters that decrease local Ca^{2+} activity, such as a discontinuous ER geometry and an increased Ca^{2+} buffering. Overall, this study proposes key parameters that regulate Ca^{2+} activity locally, potentially favoring neuron-astrocyte communication at tripartite synapses.

Introduction

Astrocytes are glial cells of the central nervous system that are essential for brain development and function, playing key roles in e.g ionic homeostasis, lactate metabolism and the uptake of neurotransmitters (see the review from Verkhratsky & Nedergaard [1] for more details). Furthermore, according to the concept of tripartite synapses [2], astrocytes take part in information processing. In response to neuronal stimulation, Ca^{2+} signals can be observed in astrocytes. The first Ca^{2+} signals that have been characterized are Ca^{2+} waves that propagate, through gap junction coupling, in astrocyte networks [3]. Ca^{2+} waves can also propagate within the branches of a single astrocyte, sporadically propagating to the soma [4, 5]. The recent development of Ca^{2+} imaging techniques that provide better spatial

and temporal resolution have revealed the existence of spatially-restricted Ca^{2+} signals in astrocytes, referred to as microdomains or hotspots [5–15]. As one astrocyte can contact $\approx$ 20,000–120,000 synapses simultaneously in the mouse hippocampus [16], up to two million in the human brain [17], those local, fast Ca^{2+} signals could enable the astrocyte to powerfully yet precisely control the flow of information through synaptic circuits.

80% of astrocyte Ca^{2+} signals, notably Ca^{2+} hotspots, occur in thin branchlets, characterized by diameters that are $<$ 200nm [5], which appear blurry when imaged using conventional light microscopy. The geometry of those compartments, forming the gliapil, has thus first been character-ized by electron microscopy (EM), which revealed their physical proximity to neurons and their complex reticular morphology [16, 18, 19]. Astro-cyte branchlets appeared to display an organized ultrastructure, forming "glial microdomains" that wrapped around synapses, potentially restrict-ing neuron-astrocyte communication [19]. This hypothesis is however hard to test experimentally because of the small size of astrocyte branchlets and because EM does not allow to study dynamical phenomena in live tissue. Recently, Arizono et al. [15] have overcome those issues by combin-ing confocal Ca^{2+} imaging and 3D-Super-Resolution Stimulated Emission Depletion (STED) microscopy. Their results suggest that the propagation of Ca^{2+} signals in astrocyte branchlets is influenced by their morphology. They notably identified bulbous structures, referred to as nodes, as pref-erential sites of Ca^{2+} activity in astrocytes. Whether there is a causal re-lationship between astrocyte branchlet morphology and the characteristics of Ca^{2+} signals however remains unclear and difficult to test experimen-tally. As Ca^{2+} microdomains might allow astrocytes to finely modulate neuronal communication at the single synapse level, elucidating the bio-physical mechanisms that regulate their formation is crucial.

Here, we use computational tools to investigate the effect of the mor-phology of astrocyte branchlets on Ca^{2+} activity. To account for the stochasticity of molecular interactions in small volumes such as those of as-trocyte branchlets, we use the voxel-based model of IP_3R-mediated Ca^{2+} signals from Denizot et al. [20]. Idealized geometries of branchlets were designed based on super-resolution microscopy images in live tissue [15]. Branchlets consist in alternations of structures referred to as nodes and shafts. Our results suggest that molecular diffusion flux decreases with shaft width, which enhances Ca^{2+} peak probability, duration and ampli-tude in the stimulated node. In case of successive node stimulation events, thin shafts allow signal propagation despite an omitted stimulus. Thin shafts thus allow more robust signal propagation. Furthermore, we pro-pose several mechanisms that decrease local Ca^{2+} activity in the gliapil: an increased shaft width, a discontinuous ER geometry and an increased Ca^{2+} buffering .

Overall, our results shed light on the mechanisms that can influence local Ca^{2+} signals in astrocyte branchlets. Importantly, our results pro-vide evidence that node compartmentalization, resulting from a reduced diffusion flux from nodes connected to thin shafts, can increase Ca^{2+} ac-tivity locally. This study provides a better understanding of the effect of the morphology of the cell and of the organelles on Ca^{2+} signals at the nanoscale.

2

Results

Geometrical representation of typical astrocyte branchlets

In order to investigate the effect of the geometry of astrocyte branchlets on the spatio-temporal properties of Ca^{2+} signals, we have designed geometries of typical astrocyte branchlets, derived from the recent characterization of their ultrastructure at high spatial resolution (50 nm in x-y) in organotypic brain slices [15]. Geometries consist in alternations of bulbous structures, nodes, connected to each other with cylindrical structures, referred to as shafts. Geometries with different shaft width d_{shaft} and constant node width were designed (Fig 1A). Screenshots of the resulting meshes are presented in Supplemental Fig S1. The geometry of the ER in the gliapil has not been characterized in live tissue so far. Thus, as a first approximation, ER geometry was considered to be identical to the geometry of the astrocyte branchlet: node/shaft successions. A sensitivity study has been performed to investigate the effect of voxel size on the kinetics of the molecular interactions modeled. Information on the voxel sizes of the different meshes used is presented in Supplemental Table S1. Results are presented in Supplemental Fig S2. Meshes that contained voxels that were $< 50 \text{nm}^3$ were characterized by aberrant kinetics, resulting in inaccurate average numbers of molecules in a given state. We have thus made sure, while meshing the geometries in which we ran the simulations, that no voxels were $< 50\ nm^3$.

3

Table 1: **Characteristics of the geometries of astrocyte branchlets used in this study.** V_{cyt} is the cytosolic volume, S_{PM} is the area of the plasma membrane and S_{ER} is the area of the ER membrane. Volumes are expressed in nm^3 and areas in nm^2.

| Geom	V_{cyt} (nm^3)	S_{PM} (nm^2)	S_{ER} (nm^2)
"5nodes" $d_{\text{shaft}} = d_0$	6.20×10^8	7.73×10^6	2.19×10^6
"5nodes" $d_{\text{shaft}} = d_0/2$	2.63×10^8	4.95×10^6	1.28×10^6
"5nodes" $d_{\text{shaft}} = d_0/3$	1.95×10^8	4.10×10^6	9.99×10^5
"No ER" $d_{\text{shaft}} = d_0$	6.73×10^8	7.73×10^6	0.00
"No ER" $d_{\text{shaft}} = d_0/2$	2.83×10^8	4.95×10^6	0.00
"No ER" $d_{\text{shaft}} = d_0/3$	2.10×10^8	4.09×10^6	0.00
"Node ER" $d_{\text{shaft}} = d_0$	6.67×10^8	7.75×10^6	4.17×10^5
"Node ER" $d_{\text{shaft}} = d_0/2$	2.74×10^8	4.96×10^6	4.37×10^5
"Node ER" $d_{\text{shaft}} = d_0/3$	2.00×10^8	4.11×10^6	4.41×10^5
"Cyl ER" $d_{\text{shaft}} = d_0$	6.27×10^8	7.74×10^6	2.03×10^5
"Cyl ER" $d_{\text{shaft}} = d_0/2$	2.77×10^8	4.95×10^6	8.78×10^5
"Cyl ER" $d_{\text{shaft}} = d_0/3$	2.07×10^8	4.09×10^6	5.86×10^5
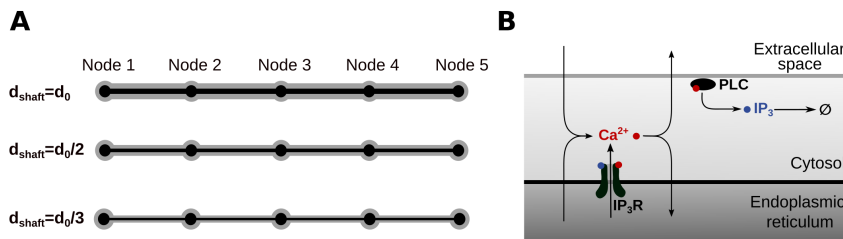
Fig 1: **Geometries and kinetic scheme used for simulating** Ca^{2+} **dynamics in node/shaft structures of the gliapil.** (*A*) Geometries reproducing node/shaft geometries of the gliapil [15, 21] were designed. Nodes are approximated as spheres of diameter 380 nm and shafts as 1μm-long cylinders. Conic geometries were added between spheres and cylinders in order to get smoother, more realistic geometries. The geometries designed in this study, referred to as "5 nodes", contain 5 identical nodes and 4 identical shafts. Geometries were characterized by different shaft widths: $d_{\text{shaft}} = d_0 = 380nm$, $d_{\text{shaft}} = \frac{d_0}{2}$ and $d_{\text{shaft}} = \frac{d_0}{3}$. The associated cytosolic volume, plasma and ER membrane areas are presented in Table 1. (*B*) Biochemical processes included in the model. Ca^{2+} can enter/exit the cytosol from/to the extracellular space or the endoplasmic reticulum (ER), resulting from the activity of Ca^{2+} channels/pumps. Ca^{2+} and IP_3 diffuse in the cytosol following Brownian motion. The kinetics of IP_3R channels corresponds to the 8-state Markov model from [22], adapted from [23, 24]. When both IP_3 and Ca^{2+} are bound to IP_3R activating binding sites, the IP_3R is in open state and Ca^{2+} enters the cytosol. Ca^{2+} can activate Phospholipase C δ (PLCδ), which results in the production of IP$_3$. For more details, please refer to [22].

Thin shafts favor node compartmentalization

In order to test whether the geometries designed in this study are a good approximation of the reticular ultrastructure of the gliapil, we have compared molecular diffusion flux in those geometries with those reported experimentally. To do so, we simulated photobleaching experiments and compared our results to experimental results from Arizono et al. [15]. The principle of bleaching simulations is presented in the Methods section and in Supplemental Fig S3. Briefly, fluorescing molecules ZSGreen encounter conformational changes at bleaching time, resulting in a decrease of the fluorescence level in the region of interest to I_0. Then, because of the diffusion of fluorescent ZSGreen into the region of interest, fluorescence increases until it reaches I_{inf} (Supplemental Movie 1). Here, we refer to a high node compartmentalization when the time to recovery after bleaching, τ, is high.

Bleaching traces in simulations are both qualitatively (Fig 2B) and quantitatively (Fig 2C) similar to experimental bleaching traces, for shaft width $d_{\text{shaft}} = d_0$ and $d_{\text{shaft}} = \frac{d_0}{2}$. Indeed, no significant difference of I_0 (Fig 2C1), I_{inf} (Fig 2C2) and τ (Fig 2C3) was observed between simulations and experimental traces. Simulations were also performed with $d_{\text{shaft}} = \frac{d_0}{3}$. Our simulations successfully reproduce experimental bleaching experiments and suggest that τ, and thus node compartmentalization, increases when shaft width decreases (Fig 2C3). This result is not surprising as a decreased shaft width results in a smaller size of the exit point for diffusing molecules from the node. This is similar to e.g dendritic spines, which compartmentalization is increased for thinner spine necks [25]. The geometries that we have designed can thus be considered as a reasonable approximation of the ultrastructure of the gliapil observed experimentally in live tissue.
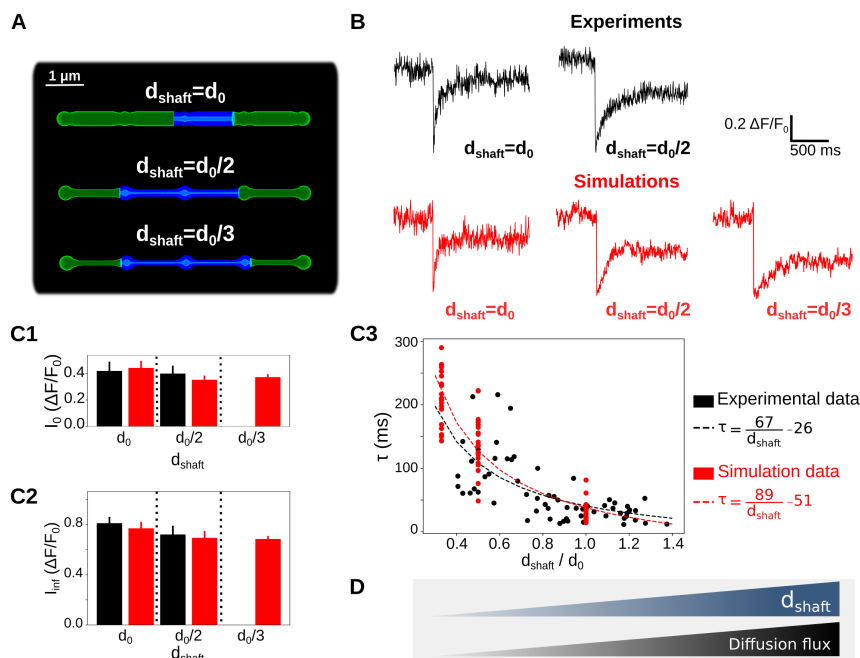
Fig 2: **Simulations confirm that thin shafts favor node compartmentalization.** (A) Geometries of different shaft widths d_{shaft}, $d_{\text{shaft}} = d_0$, $\frac{d_0}{2}$ and $\frac{d_0}{3}$, used in the bleaching simulations. Blue color represents the bleached volume, which varied depending on the value of d_{shaft} in order to fit experimental values of I_0 and I_{inf}. (B) Representative experimental (top) and simulation (bottom) traces for different shaft width values. Note that simulations were also performed for $d_{\text{shaft}} = \frac{d_0}{3}$. (C) Quantification of I_0 (C1), I_{inf} (C2) and τ (C3) values in simulations (red) compared to experiments (black). Note that no experimental data was available for $d_{\text{shaft}} = \frac{d_0}{3}$. In C1 and C2, n=5×2 and 20×3 for experiments and simulations, respectively. Data are presented as mean ± STD. In C3, n=66 and n=20×3 for experiments and simulations, respectively. τ is negatively correlated to d_{shaft} in experiments (n=66 from 7 slices; Spearman r=-0.72, p<0.001 ***) and simulations (n=60; Spearman r=-0.89, p<0.001 ***). Black and red lines represent curve fit of τ as a function of d_{shaft} of the form $\tau = a * \frac{1}{d_{\text{shaft}}} + b$ for experiments and simulations, respectively. (D) Schematic summarizing the conclusion of this figure: diffusion flux increases with d_{shaft}. In that sense, thin shafts favor node compartmentalization. Data in panels C1 and C2 are represented as mean ± STD, n=20 for each geometry.

Thin shafts are associated with increased Ca^{2+} activity in nodes

80% of astrocyte Ca^{2+} activity occurs in thin branchlets of the gliapil [5], which suggests that most neuron-astrocyte communication occurs at fine astrocyte branchlets. As we observed that a decreased shaft width is associated with a decreased diffusion flux, i.e an increased compartmentalization of nodes, we have tested whether this effect influences Ca^{2+} activity upon neuronal stimulation. To do so, we have first analyzed Ca^{2+} signals

6

resulting from the injection of IP_3 in one node (Node 1). Signals were
recorded both in the stimulated node and in the neighboring node (Node
2) (Fig 3A, Supplemental Movie 2). Representative Ca^{2+} traces in node 1
and 2 for $d_{\text{shaft}} = d_0$, $\frac{d_0}{2}$ and $\frac{d_0}{3}$ are displayed in Fig 3A. Our first notice-
able result is that Ca^{2+} peak probability increases when d_{shaft} decreases,
both in nodes 1 and 2 (Fig 3B1). The time to 1st peak increases with
d_{shaft} (Fig 3B2). On the contrary, peak amplitude (Fig 3B3) and duration
(Fig 3B4) increase when d_{shaft} decreases, both in nodes 1 and 2. Interest-
ingly, Ca^{2+} signals were not significantly different between node 1 and 2,
suggesting an "all-or-nothing" propagation to neighboring nodes. Indeed,
as soon as a Ca^{2+} peak was detected in node 1, an event of similar size
was always detected in node 2. In order to better understand the mecha-
nisms responsible for the increased Ca^{2+} peak probability, amplitude and
duration when d_{shaft} decreases, we have measured the frequency of IP_3R
opening in nodes 1 and 2. The frequency of IP_3R opening increases when
d_{shaft} decreases (Fig 3B5). Note that the duration of IP_3R opening and
the number of IP_3R open per Ca^{2+} peak did not vary with d_{shaft}. This
increase of IP_3R opening frequency when d_{shaft} decreases probably results
from the increased residency time of molecules in nodes connected to thin
shafts (Fig 3C). Indeed, a thin shaft can "trap" Ca^{2+} and IP_3 longer in
the node, thus locally increasing the probability of IP_3Rs to open, re-
sulting in larger Ca^{2+} peaks. For more details, the reader can refer to
the theoretical work investigating the narrow escape problem for diffusion
in microdomains [26]. Nodes connected to thinner shafts, despite being
characterized by a lower diffusion flux (Fig 2), could thus consist in sig-
nal amplification units, favoring the generation of larger signals, therefore
increasing Ca^{2+} peak probability, amplitude and duration both in the stim-
ulated node and in neighboring nodes.

In order to better understand the variability of Ca^{2+} signals with d_{shaft},
the effect of the volume of the astrocytic process was tested. Geometries
with $d_{\text{shaft}} = d_0$, $\frac{d_0}{2}$ and $\frac{d_0}{3}$ are characterized by node/shaft width ratios δ
of 1, 2 and 3, respectively. Those geometries are further characterized by
different volumes: $V_1=0.620$ μm^3, $V_2=0.263$ μm^3 and $V_3=0.195$ μm^3. To
test whether the effect of node/shaft width ratio δ on Ca^{2+} signals resulted
from the decreased branchlet volume with δ, a subset of simulations were
performed in a geometry with $\delta=1$ and $V_1=0.258$ μm^3, which is similar to
V_2 and V_3 (see Methods). The results are presented in Supplemental Fig
S4 and suggest that it is node/shaft width ratio rather than shaft width
itself that influences Ca^{2+} residency time in nodes. A high node/shaft
width ratio results in a higher IP_3R opening frequency and a higher peak
amplitude in nodes. Further, our results illustrate that the increase of Ca^{2+}
activity when shaft width decreases mostly results from the associated
decrease of cellular volume.

7

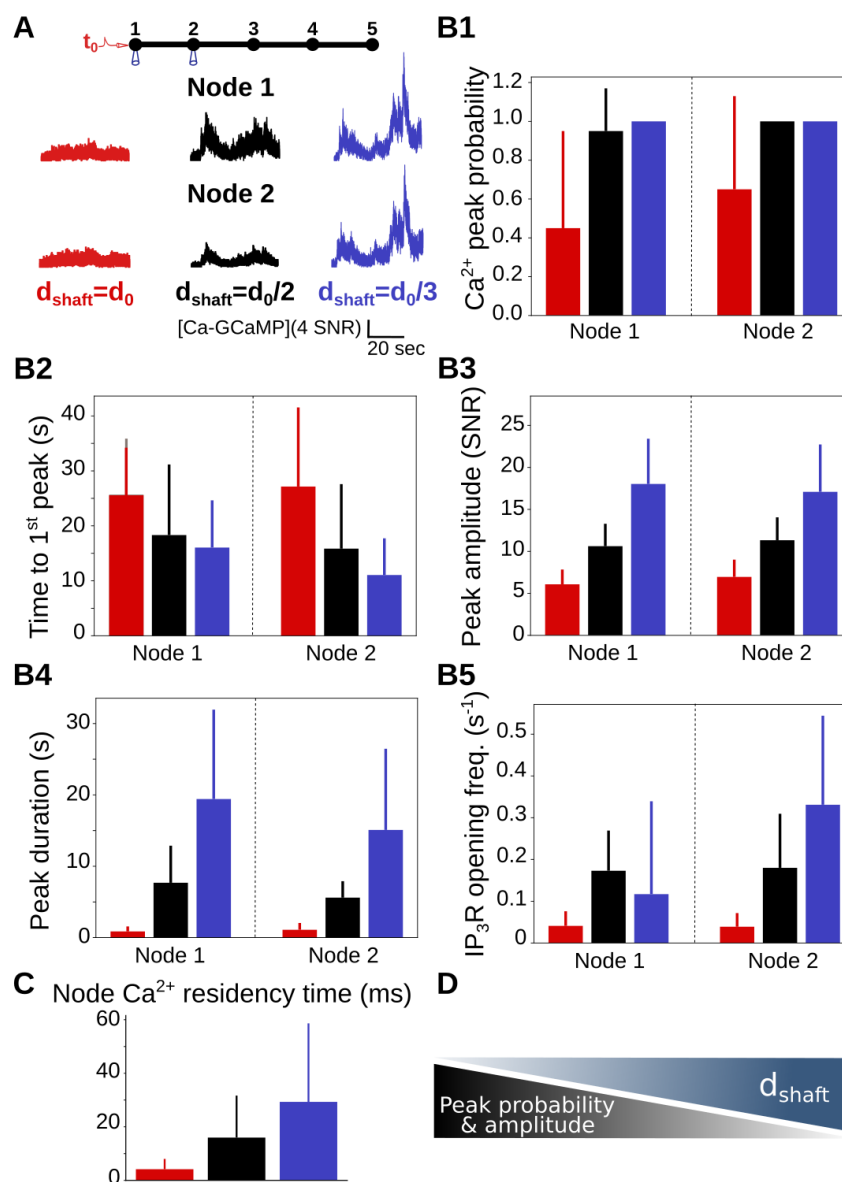Fig 3: Ca^{2+} **peak probability, amplitude and duration increase when shaft width decreases.** (A) (Top) Neuronal stimulation protocol simulated for each geometry: node 1 was stimulated at t=t_0=1s, while Ca^{2+} activity was monitored in nodes 1 and 2. Representative Ca^{2+} traces for shaft width $d_{shaft} = d_0$ (red), $\frac{d_0}{2}$ (black) and $\frac{d_0}{3}$ (blue) in node 1 ($Middle$) and node 2 ($Bottom$), expressed as SNR (see Methods). (B) Quantification of the effect of d_{shaft} on Ca^{2+} signal characteristics. Data are represented as mean ± STD, n=20 for each geometry. ($B1$) Ca^{2+} peak probability increases when d_{shaft} decreases in both node 1 and 2 (***). ($B2$) Time to 1st peak increases with d_{shaft} in both Node 2 (*) and Node 1 (***). ($B3$) Peak amplitude increases when d_{shaft} decreases in both nodes 1 and 2 (***). ($B4$) Peak duration increases when d_{shaft} decreases in both nodes 1 and 2 (***). ($B5$) The frequency of IP_3R opening increases when d_{shaft} decreases in both nodes 1 and 2 (***). Ca^{2+} peak characteristics were not statistically different between node 1 and node 2, for $d_{shaft} = d_0$, $\frac{d_0}{2}$ and $\frac{d_0}{3}$. (C) Ca^{2+} residency time in node 1 increases when d_{shaft} decreases (***, n=300). (D) Schematic summarizing the main result from this figure: Ca^{2+} peak probability and amplitude increase when shaft width decreases. The effect of d_{shaft} on each Ca^{2+} signal characteristic was tested using one-way ANOVA. Significance is assigned by * for $p \leq 0.05$, ** for $p \leq 0.01$, *** for $p \leq 0.001$.

8

In the simulations presented in Fig 3, IP_3R density was constant. As ER area varied with d_{shaft} (see Table 1) and as IP_3R density was kept constant, the total number of IP_3R molecules differed and equaled 620, 363 and 283, for $d_{shaft} = d_0$, $\frac{d_0}{2}$ and $\frac{d_0}{3}$, respectively. To test whether the effect of d_{shaft} on Ca^{2+} signals reported in Fig 3 resulted from the variation of the number of IP_3R molecules with d_{shaft}, we have performed simulations in which the number of IP_3R molecules did not vary with d_{shaft}. The results are presented in Supplemental Fig S5 and confirm that Ca^{2+} peak probability, duration and amplitude increase when d_{shaft} decreases. In order to test the effect of reflective boundary conditions, we have performed simulations in which the tetrahedra near the outer surface of Node 4 consisted in clamped boundary conditions (Supplemental Fig S6). Similarly to simulations with reflective boundary conditions, Ca^{2+} peak probability, duration and amplitude increased when d_{shaft} decreased. Simulations in which Node 3 was stimulated were also performed. Results are presented in Supplemental Fig S7. Ca^{2+} peak probability, duration and amplitude similarly increased when d_{shaft} decreased and Ca^{2+} peak characteristics were similar in Node 3 and 4.

Finally, we have tested whether the increased Ca^{2+} activity of induced signals in geometries with thin shafts could be observed for spontaneous Ca^{2+} signals. To do so, 200 Ca^{2+} ions were infused in Node 1 at time $t=t_0$, thus mimicking a Ca^{2+} signal resulting from the spontaneous opening of Ca^{2+} channels. Ca-GCaMP signals were then monitored in nodes 1 and 2. The results are presented in Supplemental Fig S8. Simulation results suggest that, similarly to neuronal-induced Ca^{2+} signals (Fig 3), peak probability, amplitude and duration increase when d_{shaft} decreases, both in nodes 1 and 2. Furthermore, the delay of Ca^{2+} peaks decreases with d_{shaft}. Cellular geometry thus affects both spontaneous and induced Ca^{2+} signals. Consistently with experimental results [15], we observe an increase of the amplitude ratio of spontaneous Ca^{2+} signals between Node 2 and Node 1 with shaft width (Spearman r=0.0006, p-value $<$ 0.001 ***). This could result from the decreased diffusion flux from nodes connected to thin shafts, so that a smaller proportion of molecules would reach the neighboring node.

Overall, our results suggest that a decreased shaft width, although resulting in a decreased diffusion flow from nodes, increases Ca^{2+} peak probability, amplitude and duration.

Discontinuous ER geometry is associated with decreased Ca^{2+} activity

As the ultrastructure of the ER in the geometries presented in Fig 1 was arbitrary, we have next investigated to what extent the effect of shaft width d_{shaft} reported in Fig 3 depends on ER geometry. To do so, we have created geometries with the same cellular geometry as in Fig 1 while varying the geometry of the ER (Fig 4A, Fig S7A). Simulations performed in the geometries used so far in this study, in which the ER consists in alternations of nodes and shafts, are here referred to as "Node/shaft ER". A subset of simulations, referred to as "Cyl ER", has been performed in meshes that contain continuous, cylindrical ER, with a length of $l_{ER}= 6274$ nm and a diameter of 108, 54 and 36 nm, for $d_{shaft} = d_0$, $\frac{d_0}{2}$ and $\frac{d_0}{3}$, respec-

252 tively. Another subset of simulations, referred to as "Node ER", contained
253 discontinuous ER, which consisted in spheres with a diameter of 54 nm, lo-
254 cated in nodes. Finally, simulations referred to as "No ER" were performed
255 without any ER. Node 1 was stimulated at $t=t_0=1s$, while Ca^{2+} activity
256 was monitored in nodes 1 and 2. Note that no signals occur in the "No
257 ER" geometry, as there are no IP_3R channels. Ca^{2+} signals qualitatively
258 (Fig 4B) and quantitatively (Fig 4C) varied depending on ER geometry.
259 Time to 1st is higher (Fig 4C2) and Ca^{2+} peak probability (Fig 4C1),
260 amplitude (Fig 4C3) and duration (Fig 4C4) as well as the frequency of
261 IP_3R opening (Fig 4C5) are lower in geometries with discontinuous com-
262 pared to continuous ER geometry. Note that IP_3R opening frequency was
263 larger in simulations in "Node ER" geometry than in "Node/shaft ER"
264 geometry with IP_3Rs located in nodes, although not resulting in any sig-
265 nificant difference of peak characteristics. Similarly to "Node/shaft" ER
266 geometry, there was no significant difference between peak characteristics
267 in Node 1 compared to Node 2 and Ca^{2+} peak probability, amplitude
268 and duration increased when d_{shaft} decreased, for all ER geometries tested
269 (Supplemental Fig S9B-C). Ca^{2+} peak probability, amplitude and dura-
270 tion were larger in "Cyl ER" geometries than in "Node ER" geometry
271 but lower than in "Node/shaft ER" geometry (Supplemental Fig S9B-C).
272 Interestingly, Ca^{2+} node residency time did not vary depending on ER
273 morphology (Supplemental Fig S10A), suggesting that the increased Ca^{2+}
274 activity in branchlets containing continuous ER might not result from ER
275 morphology itself. To further understand those results, as ER surface area
276 is increased in "Node/shaft ER" geometry compared to "Node ER" geom-
277 etry, we have tested whether the increased Ca^{2+} dynamics in branchlets
278 with continuous ER results from the associated increase of the number of
279 IP_3R channels in the branchlet. For example, there are 283 and 125 IP_3R
280 channels in "Node/shaft ER" and "Node ER" geometry with $d_{\text{shaft}}=\frac{d_0}{3}$,
281 respectively. To do so, simulations were performed in "Node/shaft ER"
282 and "Node ER" with the same amount of IP_3R channels, 300, located in
283 nodes. Ca^{2+} signals did not vary depending on ER morphology in those
284 simulations (Supplemental Fig S10B). Those results suggest that the de-
285 creased Ca^{2+} activity in branchlets with discontinuous ER mainly results
286 from the associated decreased surface area compared to continuous ER ge-
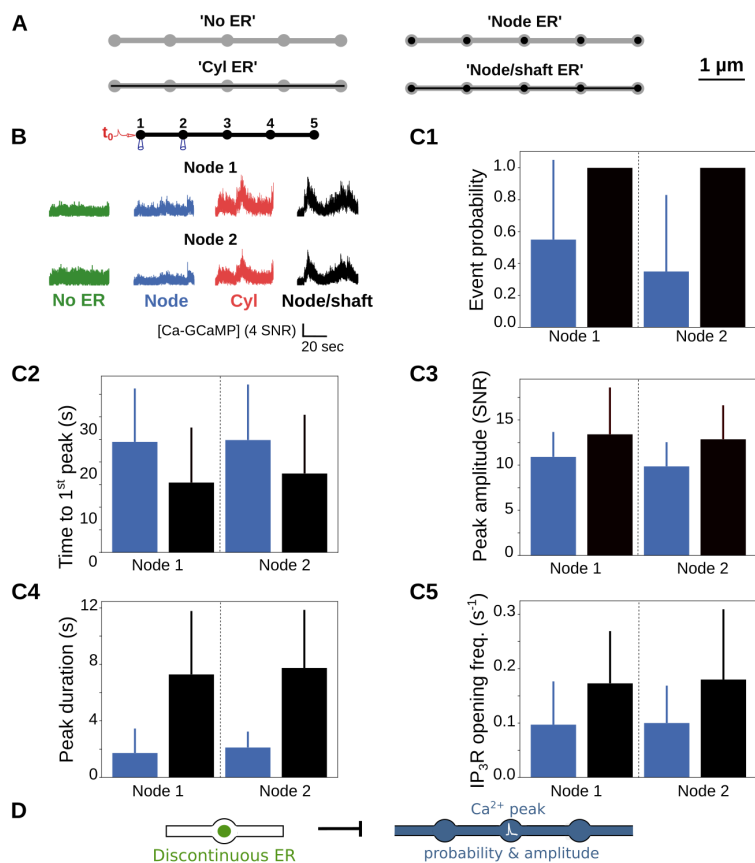287 ometries.
288

Fig 4: **ER discontinuity is associated with decreased Ca^{2+} peak probability, amplitude and duration.** (*A*) Simulations were performed in geometries with various ER geometries: "No ER", "Node ER" and "Node/shaft ER", in which there was no ER, discontinuous ER in nodes or nodes consisting in node/shaft alternations, respectively. (*B*) (*Top*) Neuronal stimulation protocol simulated for each geometry: Node 1 was stimulated at $t=t_0=1$s, while Ca^{2+} activity was monitored in nodes 1 and 2. (*Bottom*) Representative Ca^{2+} traces in nodes 1 and 2, in "No ER" (green), "Node ER" (blue) and "Node/shaft ER" (black) geometries, for $d_{shaft} = \frac{d_0}{2}$, expressed as SNR (see Methods). (*C*) Quantification of peak characteristics depending on ER geometry, $d_{shaft} = \frac{d_0}{2}$ ("Node ER" in blue and "Node/shaft" in black). (*C1*) Ca^{2+} peak probability is higher in geometries with continuous compared to discontinuous ER, both in node 1 and 2 (***). (*C2*) Time to 1st peak does not significantly change with ER geometry in Node 1 (p-value=0.59) but is higher in "Node/shaft ER" compared to "Node ER" geometry in Node 2 (p-value=0.04 *). (*C3*) Peak amplitude is increased in "Node/shaft ER" compared to "Node ER" geometry, both, both in nodes 1 and 2 (***). (*C4*) Peak duration is increased in "Node/shaft ER" compared to "Node ER" geometry, both in nodes 1 and 2 (***). (*C5*) The frequency of IP$_3$R opening is increased in "Node/shaft ER" compared to "Node ER" geometry, both in node 1 (p-value=0.01 *) and 2 (p-value=0.02 *). Ca^{2+} peak characteristics were not statistically different between node 1 and 2. (*D*) Schematic summarizing the conclusion of this figure: discontinuous ER geometry is associated with decreased Ca^{2+} peak probability and amplitude. Data are represented as mean $\pm$ STD, n=20 for each geometry. Significance is assigned by * for $p \leq 0.05$, ** for $p \leq 0.01$, *** for $p \leq 0.001$.

²⁸⁹ Overall, our simulation results highlight the effect of both cellular and
²⁹⁰ ER geometry on Ca^{2+} peak amplitude and probability. A discontinuous
²⁹¹ ER geometry is associated with a decreased peak probability, duration and
²⁹² amplitude. Those results highlight the importance of investigating the ul-
²⁹³ trastructure of intracellular Ca^{2+} stores in live tissue, as it might strongly
²⁹⁴ influence local Ca^{2+} activity in the gliapil.
²⁹⁵

Thin shafts favor more robust signal propagation

²⁹⁷ A single astrocyte branchlet can be in close contact to multiple synapses
²⁹⁸ simultaneously [15, 27–29]. The frequency of stimulation of the branchlet
²⁹⁹ could vary depending on the activity of the adjacent synapses, so that a
³⁰⁰ connection of astrocytic nodes to co-active synapses would result in a high
³⁰¹ node stimulation frequency. We have thus tested the influence of the fre-
³⁰² quency of neuronal stimulation of neighboring nodes on the propagation
³⁰³ of Ca^{2+} signals in branchlets. In order to do so, we have performed sim-
³⁰⁴ ulations in which neighboring nodes were successively stimulated after a
³⁰⁵ time period τ_{IP3}, that varied from 50 ms to 5s (Fig 5A), while Ca^{2+} sig-
³⁰⁶ nals were recorded in a remote node (Node 5). Representative Ca^{2+} traces
³⁰⁷ in Node 5 depending on shaft width d_{shaft} and on τ_{IP3} are presented in
³⁰⁸ Fig 5A. Our first noticeable result is that the time to 1st peak in Node 5
³⁰⁹ decreases with d_{shaft}, whatever the value of τ_{IP3} (Fig 5B1). More specifi-
³¹⁰ cally, time to 1st peak is higher for $d_{shaft} = d_0$ compared to both $d_{shaft} = \frac{d_0}{2}$
³¹¹ and $\frac{d_0}{3}$, while differences between $d_{shaft} = \frac{d_0}{2}$ and $\frac{d_0}{3}$ are not as striking.
³¹² Moreover, the difference between $d_{shaft} = d_0$, $\frac{d_0}{2}$ and $\frac{d_0}{3}$ increases with τ_{IP3}.
³¹³ This suggests that geometries with $d_{shaft} = d_0$ better discriminate slow from
³¹⁴ fast frequency of node stimulation compared to geometries with thinner
³¹⁵ shafts. Geometries with $d_{shaft} = d_0$ are further characterized by a lower
³¹⁶ Ca^{2+} peak probability in Node 5 compared to geometries with $d_{shaft} = \frac{d_0}{2}$
³¹⁷ and $\frac{d_0}{3}$ (Fig 5B2). More precisely, Ca^{2+} peak probability decreases as τ_{IP3}
³¹⁸ increases for $d_{shaft} = d_0$. This suggests that geometries with larger shafts
³¹⁹ could be associated with decreased signal propagation to remote nodes in
³²⁰ case of successive node stimulation at low frequency ($\tau_{IP3} > 2s$). In order
³²¹ to test the effect of our reflective boundary conditions, we have performed
³²² the same stimulation protocol in geometries in which the tetrahedra near
³²³ the outer surface of Node 4 formed clamped boundary conditions (Supple-
³²⁴ mental Fig S11). The effect of d_{shaft} and of τ_{IP3} on Ca^{2+} peak probability
³²⁵ and on the delay of signal onset was similar to simulations with reflective
³²⁶ boundaries. Note that Ca^{2+} peak probability was lower and time to 1st
³²⁷ peak higher compared to simulations with reflective boundary conditions.
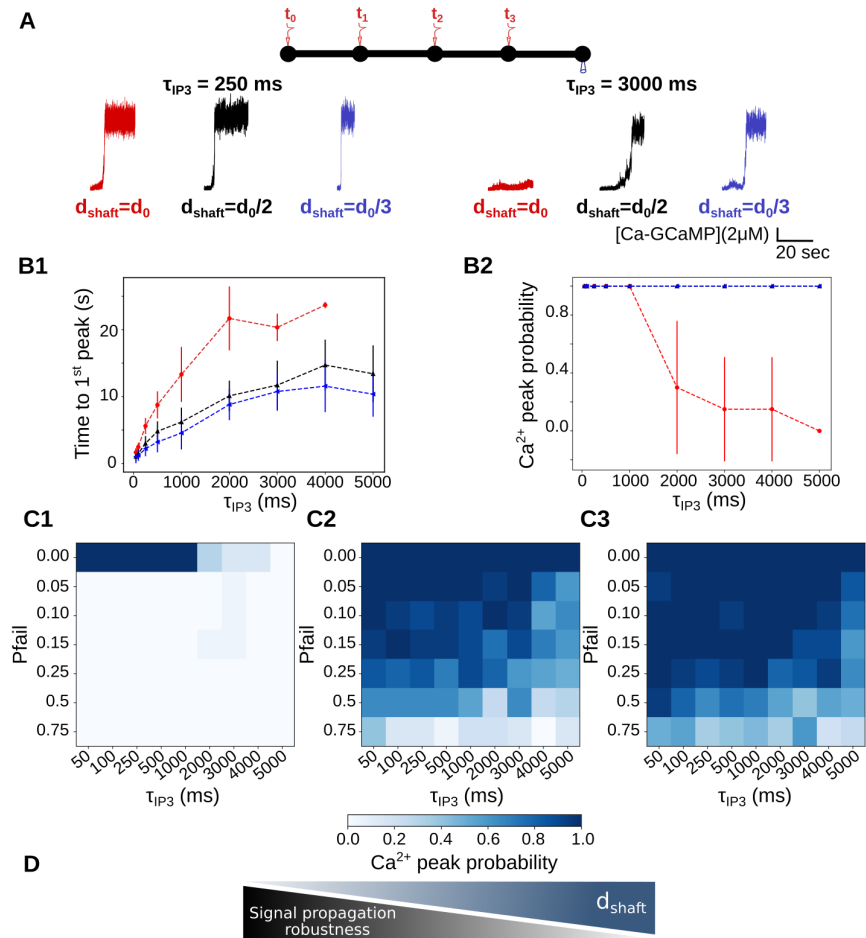³²⁸

Fig 5: **Thin shafts are associated with a more robust signal propagation upon successive neuronal stimuli.** (A) (Top) Neuronal stimulation protocol: Node 1 is stimulated at t=t_0=5s, Node 2 at $t_0 + \tau_{IP3}$, Node 3 at $t_0 + 2\tau_{IP3}$ and Node 4 at $t_0 + 3\tau_{IP3}$. Ca^{2+} activity is recorded in Node 5. ($Bottom$) Representative Ca^{2+} traces in Node 5 for shaft width $d_{shaft} = d_0$ (red), $\frac{d_0}{2}$ (black) and $\frac{d_0}{3}$ (blue), with τ_{IP3}=250ms (left) and 3000ms (right), expressed as SNR (see Methods). ($B1$) Time to 1st peak increases with τ_{IP3} for d_{shaft}=d_0 (***), $\frac{d_0}{2}$ (***) and $\frac{d_0}{3}$ (***). T-tests revealed that for any value of τ_{IP3}, time to 1st peak is higher for d_{shaft}=d_0 compared to d_{shaft}=$\frac{d_0}{2}$ and $\frac{d_0}{3}$. Time to 1st peak is significantly higher when d_{shaft}=$\frac{d_0}{2}$ compared to d_{shaft}=$\frac{d_0}{3}$, for most values of τ_{IP3} (p=0.032 *, 0.0025 **, 0.034 *, 0.016 * and 0.019 * for τ_{IP3}=250, 500, 1000, 4000 and 5000, respectively). ($B2$) Ca^{2+} peak probability in Node 5 is lower for d_{shaft}=d_0 compared to d_{shaft}=$\frac{d_0}{2}$ and $\frac{d_0}{3}$. Ca^{2+} peak probability decreases as τ_{IP3} increases for d_{shaft}=d_0 (***). (C) Ca^{2+} peak probability in Node 5 (colorbar) as a function of τ_{IP3} and of the probability of failure of node stimulation p_{fail}, for d_{shaft}=d_0 (C1), d_{shaft}=$\frac{d_0}{2}$ (C2) and d_{shaft}=$\frac{d_0}{3}$ (C3), with $p_{fail} \in [0, 1]$. (D) Schematic summarizing the main conclusion of this figure: decreased shaft width allows signal propagation despite omitted node stimulation, thus favoring more robust signal propagation. Data are represented as mean $\pm$ STD, n=20 for each value of d_{shaft} and of τ_{IP3}. Lines in panel B are guides for the eyes. The effect of d_{shaft} on each Ca^{2+} signal characteristic was tested using one-way ANOVA. Significance is assigned by * for $p \leq 0.05$, ** for $p \leq 0.01$, *** for $p \leq 0.001$.

13

329   For τ_{IP3}=4s and $d_{\mathrm{shaft}}=\frac{d_0}{3}$, signals were detected in Node 5 11.55 $\pm$
330 3.89 s after the stimulation of Node 1, which means that they occurred
331 before the stimulation of Node 4 (t=t_0 + 12s for τ_{IP3}=4s). This phe-
332 nomenon was not observed for d_{shaft}=d_0, for which time to 1$^{\mathrm{st}}$ peak when
333 τ_{IP3}=4s was 23.67 $\pm$ 0.47 s. This suggests that for $d_{\mathrm{shaft}}=\frac{d_0}{3}$, contrary
334 to d_{shaft}=d_0, one node stimulation could be omitted without having any
335 consequence on Ca^{2+} peak probability in Node 5. In order to test this hy-
336 pothesis, we have performed simulations in which the stimulation of Nodes
337 2, 3 and 4 occurred with a given probability of failure p_{fail}. Simulations
338 were performed for p_{fail}=0, 0.05, 0.1, 0.15, 0.25 and 0.75. Ca^{2+} peak prob-
339 ability in Node 5, depending on p_{fail} and on τ_{IP3} is presented in Fig 5C, for
340 d_{shaft}=d_0 (Fig 5C1), $d_{\mathrm{shaft}}=\frac{d_0}{2}$ (Fig 5C2) and $d_{\mathrm{shaft}}=\frac{d_0}{3}$(Fig 5C3). As ex-
341 pected, Ca^{2+} peak probability, despite high values of p_{fail}, increases when
342 d_{shaft} decreases. Thus, thin shafts can favor signal propagation by allowing
343 the omission of a node stimulation. In that sense, geometries displaying
344 thin shafts are characterized by a more robust signal propagation (Fig 5D).
345

346   Together, our results suggest that, in the context of successive node
347 stimulation, thin shafts are associated with an increase of Ca^{2+} peak prob-
348 ability in more remote nodes, with a lower delay of signal onset, suggest-
349 ing an increased signal propagation. Geometries with thick shafts (here
350 d_{shaft}=d_0) are associated with lower signal propagation in case of low stim-
351 ulation frequency (time period > 2s), potentially favoring the formation of
352 local Ca^{2+} hotspots. Our results further suggest that geometries with thick
353 shafts could impair signal propagation when a branchlet is stimulated by
354 different neuronal populations. In that sense, astrocyte branchlets with
355 thick shafts would be better detectors of the surrounding neuronal stimuli.
356 On the contrary, branchlets with thin shafts would allow less discriminating
357 and more robust signal propagation events.

358 Ca^{2+} indicators alter Ca^{2+} peak characteristics

359   In order to measure Ca^{2+} signals, experiments rely on the use of Ca^{2+}
360 indicators, such as GCaMP, which correspond to molecules that fluoresce
361 when bound to Ca^{2+}. The variations of fluorescence with time are moni-
362 tored and normalized over the basal level of fluorescence ($\Delta\mathrm{F}/F_0$). Those
363 methods thus do not measure the exact variations of free Ca^{2+} concentra-
364 tion [Ca^{2+}] but the variations of the concentration of Ca^{2+} bound to the
365 indicator, here [Ca-GCaMP]. The resulting signal strongly depends on the
366 concentration and kinetics of the indicator [20].
367 Here, in order to investigate the effect of d_{shaft} on free Ca^{2+} signals rather
368 than on signals mediated by GCaMP, we have performed simulations in
369 which no GCaMP molecules were added in the cytosol. Free Ca^{2+} dynam-
370 ics was then monitored in node 1, while stimulating node 1 (Fig 6A). Free
371 Ca^{2+} signals were qualitatively (Fig 6A) and quantitatively (Fig 6B) differ-
372 ent from Ca-GCaMP signals. No effect of d_{shaft} was observed on free Ca^{2+}
373 peak probability (Fig 6B1). Similarly to Ca-GCaMP signals, time to 1st
374 peak decreased (Fig 6B2), IP$_3$R opening frequency (Fig 6B5), free Ca^{2+}
375 peak amplitude (Fig 6B3) and duration (Fig 6B4) increased when d_{shaft}
376 decreased. Consistently with previous reports [20,30,31], free Ca^{2+} signals
377 strongly differed from Ca-GCaMP signals. More precisely, free Ca^{2+} sig-
378 nals were characterized by a higher peak amplitude and frequency of IP$_3$R
379 opening as well as a lower peak duration and delay of peak onset than

14

380 Ca-GCaMP signals.

381 Overall, our results suggest that the use of Ca^{2+} indicators, and more
382 generally Ca^{2+} buffering, is associated with an increased Ca^{2+} peak dura-
383 tion and a decreased peak probability and amplitude (Fig 6D). Note that,
384 even though free Ca^{2+} signals strongly differ from Ca-GCaMP signals,
385 Ca-GCaMP signals can still provide relevant information on the qualita-
386 tive effect of shaft width on Ca^{2+} dynamics, such as the increased peak
387 probability, duration and amplitude when d_{shaft} decreases. As it is cur-
388 rently impossible to measure free Ca^{2+} signals experimentally, our study
389 highlights the importance of using computational tools for improving our
390 understanding of Ca^{2+} signals.

15
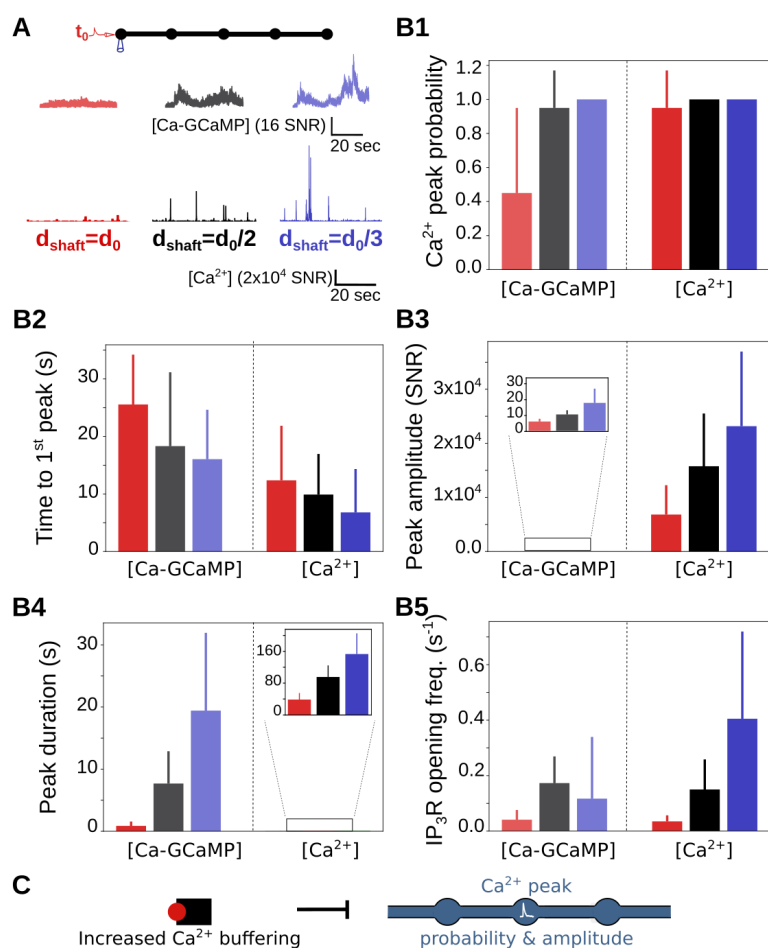
Fig 6: Ca^{2+} indicators alter Ca^{2+} peak probability, duration and amplitude. (*A*) In order to investigate free Ca^{2+} peak probability, no GCaMP molecules were added to the model. (*Top*) At $t=t_0=1s$, Node 1 was stimulated while Ca^{2+} concentration was monitored in node 1. (*Middle*) Representative Ca-GCaMP traces in node 1, in simulations containing GCaMP molecules in geometries with shaft width $d_{\text{shaft}} = d_0$ (light red), $\frac{d_0}{2}$ (grey) and $\frac{d_0}{3}$ (light blue). (*Bottom*) Representative free Ca^{2+} traces in node 1, in the absence of GCaMP molecules, in geometries with shaft width $d_{\text{shaft}} = d_0$ (red), $\frac{d_0}{2}$ (black) and $\frac{d_0}{3}$ (blue). The amplitude of Ca-GCaMP and free Ca^{2+} signals is expressed as SNR (see Methods). (*B*) Characteristics of free Ca^{2+} signals depending on d_{shaft}. Ca-GCaMP signals measured in simulations from Fig 3 are presented for comparison. (*B1*) Free Ca^{2+} peak probability does not vary with d_{shaft} (p-value=0.22). Ca-GCaMP peak probability is lower than free Ca^{2+} peak probability for $d_{\text{shaft}} = d_0$ (***). (*B2*) Time to 1st free Ca^{2+} peak increases with d_{shaft} (***). Time to 1st Ca-GCaMP peak is higher than time to 1st free Ca^{2+} peak, for any value of d_{shaft} (***). (*B3*) Free Ca^{2+} peak amplitude increases when d_{shaft} decreases (***). Ca-GCaMP peak amplitude is lower than free Ca^{2+} peak amplitude, for any value of d_{shaft} (***). (*B4*) Free Ca^{2+} peak duration increases when d_{shaft} decreases (***). Ca-GCaMP peak duration is higher than free Ca^{2+} peak duration, for any value of d_{shaft} (***). (*B5*) The frequency of IP_3R opening increases when d_{shaft} decreases (***). (*C*) Schematic summarizing the main result from this figure: increased Ca^{2+} buffering is associated with decreased Ca^{2+} peak probability and amplitude. Data are represented as mean $\pm$ STD, n=20 for each geometry. The effect of d_{shaft} on each free Ca^{2+} signal characteristic was tested using one-way ANOVA. Significance is assigned by * for $p \leq 0.05$, ** for $p \leq 0.01$, *** for $p \leq 0.001$.

Discussion

This study outlines the effect of the nanoscale morphology of astrocyte branchlets on the characteristics of Ca^{2+} signals. More precisely, the reticular morphology of branchlets, alternating between large and thinner cellular compartments [15, 19, 21], seems to increase Ca^{2+} peak probability, duration, amplitude and propagation (Fig 7A). We further propose plausible mechanisms that are associated with a decreased local Ca^{2+} activity: an increased shaft width, discontinuous ER geometry and increased Ca^{2+} buffering (Fig 7B). Our results, in accordance with experimental data, suggest that thin shafts are associated with a decreased diffusion flux, i.e an increased compartmentalization of nodes. Thus, nodes, similarly to dendritic spines [25], act as diffusion traps when shaft width is low. Note that, more than the value of shaft width itself, our results emphasize the effect of the ratio between node and shaft diameter on Ca^{2+} activity. The geometries designed and used in this study, based on recent super-resolution images of the gliapil [15], emerge as interesting tools to investigate the influence of the ultrastructure of fine astrocyte branchlets on the local Ca^{2+} dynamics. By recording Ca^{2+} activity upon neuronal stimulation in small cellular compartments of the gliapil, which cannot be performed experimentally, our simulation results shed light on the mechanisms by which astrocyte morphology influences the frequency, amplitude and propagation of Ca^{2+} signals at the nanoscale.
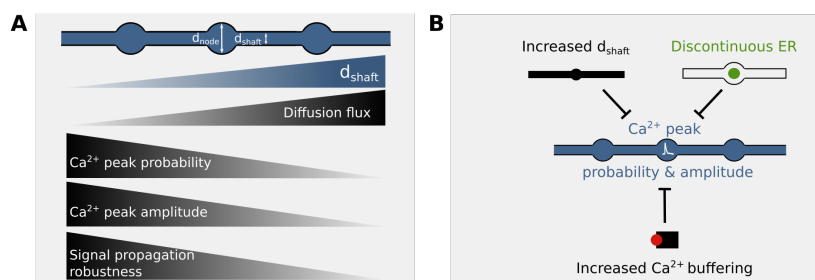

Fig 7: **Proposed mechanisms that regulate astrocytic Ca^{2+} activity at tripartite synapses.** (*A*) Proposed effects of shaft width d_{shaft} on Ca^{2+} signals. A decreased shaft width results in a decreased diffusion flux of molecules from nodes. This results in an increase of Ca^{2+} peak probability, amplitude and duration in the stimulated node . Finally, thinner shafts allow signal propagation despite omitted node stimulation upon successive stimuli, thus allowing more robust signal propagation. (*B*) Proposed mechanisms that decrease Ca^{2+} peak probability and amplitude: an increased shaft width d_{shaft}, a discontinuous ER geometry and an increased Ca^{2+} buffering.

Experimental Ca^{2+} recordings of astrocyte activity suggest that astrocyte branchlets display both highly localized microdomain signals and propagating Ca^{2+} waves [5, 9]. Our simulations suggest that the morphology of the cell and of its organelles can influence the formation of those diverse spatio-temporal properties. Notably, thinner shafts allow less discriminating and more robust signal propagation upon successive stimuli

17

420 compared to larger shafts. Thinner shafts indeed allow signal propagation
421 despite the omission of some stimuli or when the time interval between
422 successive stimuli is large. On the contrary, geometries with thick shafts
423 seem to be more discriminating, potentially favoring the propagation of
424 signals resulting from successive stimuli from co-active synapses. Cellular
425 morphology thus emerges as a key parameter that regulates the active prop-
426 agation of Ca^{2+} signals. Further quantification is required to better charac-
427 terize the inter- and intra-cellular variability of the ultrastructure of astro-
428 cyte branchlets and of its connectivity to the neighboring synapses. This
429 will be crucial to better understand the integration of signals within astro-
430 cytes and how specialized their communication with individual synapses is.

432 In neurons, both experimental [32–34] and modelling [25, 35–41] stud-
433 ies have suggested that spine morphology, more precisely thin neck width,
434 favors the compartmentalization of Ca^{2+} signals within single spine heads.
435 It has been proposed that the presence of small compartments, such as
436 astrocyte nodes and spine heads, enables a 2 orders of magnitude faster
437 homogenization of the concentration of second messengers, such as Ca^{2+},
438 compared to larger compartments [32]. According to our simulation re-
439 sults, nodes connected to thin shafts could favor the emergence of large
440 signals at the site of neuron-astrocyte communication. Interestingly, we
441 further propose that those amplified signals in nodes, instead of resulting
442 in Ca^{2+} hostpots, favor active signal propagation. In response to spike
443 timing-dependent plasticity (STDP) protocols [42] and after long-term po-
444 tentiation [34], the neck of dendritic spines become wider and shorter.
445 Recent *in vitro* and *in vivo* studies have reported that the geometry of the
446 ER in neurons is also highly dynamic [43], experiencing fast fission and
447 fusion events. The geometries of dendrites and of their organelles, which
448 influence local signals, are thus highly dynamic. Further, the ER is variably
449 distributed in spines, being preferentially present in large spines associated
450 with strong synapses [44]. The variability of the geometry of astrocyte
451 branchlets and of their organelles depending on physiological conditions
452 remains to be uncovered and, according to our results, could strongly im-
453 pact Ca^{2+} dynamics.

455 Genetically encoded Ca^{2+} indicators (GECI) have been used exten-
456 sively to investigate Ca^{2+} dynamics in astrocytes. They are presently the
457 best tools for detecting Ca2+ signals in the whole astrocyte territory, in-
458 cluding the very fine distal branchlets, while bulk-loading of Ca^{2+} indica-
459 tors can only report signals in the soma and major branches, leaving $\approx 90\%$
460 of astrocyte area unsampled [10, 45]. Furthermore, using GECIs avoids the
461 risk of altered cell physiology associated with bulk-loading [46] and can be
462 used to image Ca^{2+} signals *in vivo* [5, 9, 10, 14, 47]. GECIs however present
463 a major drawback: as they are genetically encoded, their exact concen-
464 tration and distribution within the cell is unknown and thus generally
465 not reported. Our results, in agreement with previous reports [20, 48, 49],
466 highlight the modulation of Ca^{2+} signals by Ca^{2+} buffers such as GECIs.
467 Interestingly, the increased Ca^{2+} peak probability, duration and ampli-
468 tude of Ca-GCaMP peaks when d_{shaft} decreases was still observed for free
469 Ca^{2+} signals. As the concentration of GCaMP, [GCaMP], can influence
470 the size of Ca-GCaMP peaks [20], we have tested the sensitivity of our
471 results to [GCaMP] (Supplemental Fig S12). The amplitude and duration
472 of Ca-GCaMP signals varied with [GCaMP], in accordance with previous

18

reports [20]. Importantly, the increase of peak amplitude and duration as well as the decrease of time to 1st peak when d_{shaft} decreases was observed for all tested values of [GCaMP]. This study highlights the importance of computational tools to investigate free Ca^{2+} signals and to quantify the effect of Ca^{2+} indicators on signal readout.

Overall, our simulations illustrate how the morphology of fine astrocyte branchlets, notably shaft width, and of their organelles influence local Ca^{2+} activity. Importantly, this study highlights the counter-intuitive signal amplification in compartmentalized nodes, resulting from a reduced diffusion flux from nodes connected to thin shafts. This study provides a better understanding of the mechanisms that govern Ca^{2+} dynamics in small volumes, which is notably crucial for disentangling neuron-astrocyte communication at tripartite synapses.

Methods

Stochastic spatially-explicit voxel-based simulations

In order to model astrocyte Ca^{2+} signals in astrocyte branchlets, we have used the voxel-based "GCaMP" implementation of the Inositol 3-Phosphate (IP_3) receptor-dependent Ca^{2+} signaling model from Denizot et al [20], using the same reaction scheme and parameter values (Fig 1B). Briefly, we model Ca^{2+} fluxes in and out of the cytosol, mediated by Ca^{2+} channels and pumps on the endoplasmic reticulum (ER) and on the plasma membrane. Ca^{2+} signals occur when some IP_3R channels are in the open state. IP_3 can be synthesized by the Ca^{2+}-dependent activity of phospholipase C δ (PLCδ) and the removal of IP_3 molecules from the cytosol is expressed as a single decay rate. IP_3R kinetics is described by a Markov model, derived from De Young & Keizer's model [23]. Each IP_3R molecule contains one IP_3 binding site and two Ca^{2+} binding sites. An IP_3R is in the open state when in state {110} (first Ca site and IP_3 bound, second Ca site free). Depending on the simulation, other diffusing molecules were added to the model, such as the fluorescent molecule ZSGreen and fluorescent Ca^{2+} indicators, here 10 μM of GCaMP6s. GCaMPs are genetically-encoded Ca^{2+} indicators (GECIs) that are derived from the fluorescent protein GFP and the Ca^{2+} buffer calmodulin (see [50] for a review on GECIs). For further details on the kinetic scheme and model assumptions, please refer to Denizot et al. 2019 [20].

The model was implemented using STEPS (http://steps.sourceforge.net/), a python package performing exact stochastic simulation of reaction-diffusion systems [51]. More presicely, STEPS uses a spatialized implementation of Gillespie's SSA algorithm [52–54]. Simulations in STEPS can be performed in complex geometries in 3 spatial dimensions. Space is divided into well-mixed tetrahedral compartments, referred to as voxels. Reactions between 2 molecules can only occur if they are located within the same voxel. Diffusion events are modeled as a decrease of the number of molecules in the original voxel and an increase in the number of molecules in its neighboring voxel. Boundary conditions, except when specified otherwise, were reflective. STEPS enables to compute, in complex 3D geometries, reactions and diffusion in the cytosol as well as reactions between cytosolic molecules and molecules located at the plasma or ER membrane.

523

Geometries

Typical astrocyte branchlet geometries were designed from their recent experimental characterization in live tissue at high spatial resolution (50 nm in x-y) [15]. Those geometries consist in alternations of bulbous structures, nodes, connected to each other with cylindrical structures, shafts. Geometries with different shaft widths d_{shaft} were designed using Trelis software (https://www.csimsoft.com/trelis, Fig 1A). The geometry of a node was approximated as being a sphere of diameter 380 nm. Shaft geometry consisted in a 1μm long cylinder. Shaft diameter was defined relative to node diameter. For example, shaft diameter was the same as node diameter, i.e $d_{\text{shaft}} = d_0 = 380$ nm. Similarly, shaft diameter was 190 nm and 127 nm for $d_{\text{shaft}} = \frac{d_0}{2}$ and $\frac{d_0}{3}$, respectively. Cones were positioned between spheres and cylinders in order to create a smoother transition between nodes and shafts, better approximating the geometry observed experimentally. Cytosolic volume was thus $V_1 = 0.620 \ \mu m^3$, $V_2 = 0.263 \ \mu m^3$ and $V_3 = 0.195 \ \mu m^3$, for $d_{\text{shaft}} = d_0$, $\frac{d_0}{2}$ and $\frac{d_0}{3}$, respectively. A subset of simulations were performed in a geometry with $V_1 = 0.258 \ \mu m^3$. This geometry is characterized, similarly to geometries with $d_{\text{shaft}} = d_0$, by a node/shaft width ratio of 1. It contains cylinders of length 750 nm, diameter 285 nm and spheres of diameter 285 nm. As a first approximation, ER geometry was considered to be identical to the geometry of the astrocyte branchlet: node/shaft successions. ER nodes were aligned with cytosolic nodes. As no quantification of the ER volume compared to cellular volume was found for astrocytes in the literature, ER volume was 10% of the total branchlet volume, based on available data in neurons [55]. The cytosolic volume, plasma and ER membrane areas of the different "5Nodes" geometries are presented in Table 1.

In a subset of simulations, ER geometry varied. The shape of the cell was the same as in "5nodes" geometries (Fig 1). ER geometry consisting of node/shaft alternations, described above, is referred to as "Node/shaft ER". "No ER" geometry contains no ER. "Node ER" is characterized by a discontinuous ER geometry, consisting in spheres of diameter 54 nm, located in cellular nodes. "Cyl ER" corresponds to a cylindrical ER, of length $l_{\text{ER}} = 6274$ nm and a diameter of 108, 54 and 36 nm, for $d_{\text{shaft}} = d_0$, $\frac{d_0}{2}$ and $\frac{d_0}{3}$, respectively. The associated cytosolic volume, ER and plasma membrane area are presented in Table 1.

Protocol for simulating bleaching experiments

In order to test whether the idealized geometries presented in Fig 1 are a good approximation of the spongiform ultrastructure of astrocyte branchlets, we have simulated their fluorescence recovery after photobleaching (FRAP) experiments. The principle of those experiments is summarized in Supplemental Fig S3A. Briefly, laser pulses are simulated on a node (region of interest) while the fluorescence level is being recorded. At bleaching time, the fluorescence level in the region of interest decreases to I_0. Then, because of the diffusion of fluorescent molecules into the region of interest, fluorescence increases until it reaches a new steady state, I_{inf}. We characterize node compartmentalization by measuring the time τ taken by fluorescing molecules to diffuse into the node to reach I_{inf}. In other words,

20

a high node compartmentalization will be associated with a high value of τ. Thus, 3 main parameters characterize bleaching traces: I_0, τ and I_{inf}.

To mimic bleaching experiments in fine branchlets performed by Arizono et al [15], ZSGreen molecules were added to simulation space. After 2 seconds of simulation, providing the basal level of fluorescence, 60% of ZSGreen molecules were bleached. In order to fit I_0 and I_{inf} that were measured experimentally, and as bleaching time lasted 10 ms in experiments and 1 ms in simulations, the bleached volume in simulations was adjusted depending on the geometry (see Fig 2A). Bleaching was simulated as a transition from ZSGreen molecules to ZSGreen-bleached molecules, the latter being considered as non-fluorescing molecules. Screenshots of simulations, illustrating the diffusion of ZSGreen and ZSGreen-bleached molecules, are presented in Fig S2B. The number of ZSGreen molecules in the central node was recorded over simulation time and a fit was performed following equation 1 to determine the values of I_0, I_{inf} and τ.

$$I(t) = I_0 - (I_0 - I_{\mathrm{inf}})e^{-t/\tau} \tag{1}$$

, where I(t) is the level of fluorescence measured at time t. The coefficient of diffusion, D_{ZSGreen}, and the concentration, [ZSGreen], of ZSGreen were adjusted to fit experimental data. Indeed, the amplitude of [ZSGreen] fluctuations at steady state is inversely proportional to the number of ZSGreen molecules in the geometry. In other words, fluorescence signals are more noisy when [ZSGreen] is low. Moreover, the autocorrelation of those fluctuations depends on the coefficient of diffusion of ZSGreen, D_{ZSGreen}. If D_{ZSGreen} increases, the autocorrelation of Lag, where Lag is the autocorrelation delay, will decrease faster as Lag increases. Comparing the fluctuations of [ZSGreen] and its autocorrelation in experiments and in simulations thus enabled to find the values of D_{ZSGreen} and of [ZSGreen] that allowed for the best fit to experimental data. In the simulations presented here, D_{ZSGreen}=90 $\mu m^2.s^{-1}$ and [ZSGreen]=25 μM.

Protocols for simulating neuronal stimulation

In order to investigate the propagation of Ca^{2+} signals from nodes that contact neuronal spines, we have developed 2 different protocols for our simulations, performed in the geometries presented in Fig 1. As nodes were the site of Ca^{2+} signal initiation [15] and as most spines contacted nodes rather than shafts, we have simulated neuronal stimulation in nodes.

- In the first protocol, 100 IP$_3$ molecules were infused in Node 1, at t=t_0=1s, while Ca^{2+} activity was monitored in Node 1 and in the neighboring node, Node 2 (see e.g Fig 3A). Simulations were performed in geometries with varying shaft width d_{shaft} .

- In the second protocol, we have investigated signal propagation in the node/shaft geometry depending on shaft width d_{shaft} when several nodes were successively stimulated. In "5nodes" geometries, 50 IP$_3$ molecules were infused at t_0=5s, $t_0 + \tau_{\mathrm{IP3}}$, $t_0 + 2\tau_{\mathrm{IP3}}$, $t_0 + 3\tau_{\mathrm{IP3}}$ in Nodes 1, 2, 3 and 4, respectively. During the whole simulation time, Ca^{2+} activity was recorded in Node 5 (see Fig 5). In a subset of simulations, stimulation of Nodes 2, 3 and 4 occurred with a probability $1 - p_{\mathrm{fail}}$, with $p_{\mathrm{fail}} \in [0, 1]$.

21

Peak detection and analysis

The same strategy as developed by Denizot et al. [20] was used for detecting and analysing Ca^{2+} signals. Briefly, basal concentration of Ca^{2+}, $[Ca]_b$, was defined based on a histogram of the number of Ca^{2+} ions in the absence of neuronal stimulation. Peak initiation corresponded to the time when $[Ca^{2+}]$ was higher than the following threshold: $[Ca]_b + n\sigma_{Ca}$, where σ_{Ca} is the standard deviation of $[Ca^{2+}]$ histogram in the absence of neuronal stimulation. The value of n was set by hand depending on signal/noise ratio of the simulation of interest. Peak termination corresponded to the time when $[Ca^{2+}]$ decreased below the peak threshold. Several parameters were analyzed to characterize Ca^{2+} signals. Peak amplitude, A, corresponds to the maximum $[Ca^{2+}]$ measured during the peak duration. It is expressed as signal to noise ratio $SNR = \frac{A-[Ca]_b}{[Ca]_b}$. Peak duration corresponds to the time between peak initiation and peak termination. Time to 1st peak corresponds to the delay between the beginning of the simulation and the first peak detection, measured in the cellular compartment of interest. Peak probability corresponds to the fraction of simulations in which at least one peak was detected during simulation time in the region of interest. Ca^{2+} residency time was measured by performing n=300 simulations for each value of d_{shaft}, in which only 1 Ca^{2+} ion was added to node 1, without other molecular species. Ca^{2+} residency time corresponds to the time taken for the ion to diffuse away from node 1.

Statistical analysis

For each parameter set, 20 simulations, with different seeds, were generated. Each parameter describing Ca^{2+} dynamics was expressed as mean $\pm$ standard deviation. The effect of d_{shaft} on each Ca^{2+} signal characteristic was tested using one-way ANOVA. Comparison between two different conditions was performed using unpaired Student T-test if values followed a Gaussian distribution, Mann-Whitney test otherwise. Significance is assigned by * for $p \leq 0.05$, ** for $p \leq 0.01$, *** for $p \leq 0.001$.

Simulation code

The simulation code, implemented with STEPS 3.5.0, and the meshes are available on ModelDB [56] at http://modeldb.yale.edu/266928, access code: lto42@tpk3D?. The original model from Denizot et al. [20] is available at http://modeldb.yale.edu/247694.

References

[1] A. Verkhratsky and M. Nedergaard, "Physiology of Astroglia," *Physiological Reviews*, vol. 98, pp. 239–389, Jan. 2018.

[2] A. Araque, V. Parpura, R. P. Sanzgiri, and P. G. Haydon, "Tripartite synapses: glia, the unacknowledged partner," *Trends in Neurosciences*, vol. 22, pp. 208–215, May 1999.

[3] C. Giaume and L. Venance, "Intercellular calcium signaling and gap junctional communication in astrocytes," *Glia*, vol. 24, pp. 50–64, Sept. 1998.

[4] M. D. Haustein, S. Kracun, X.-H. Lu, T. Shih, O. Jackson-Weaver, X. Tong, J. Xu, X. W. Yang, T. J. O'Dell, J. S. Marvin, M. H. Ellisman, E. A. Bushong, L. L. Looger, and B. S. Khakh, "Conditions and constraints for astrocyte calcium signaling in the hippocampal mossy fiber pathway," *Neuron*, vol. 82, pp. 413–429, Apr. 2014.

[5] E. Bindocci, I. Savtchouk, N. Liaudet, D. Becker, G. Carriero, and A. Volterra, "Three-dimensional Ca^{2+} imaging advances understanding of astrocyte biology," *Science*, vol. 356, p. eaai8185, May 2017.

[6] M. A. Di Castro, J. Chuquet, N. Liaudet, K. Bhaukaurally, M. Santello, D. Bouvier, P. Tiret, and A. Volterra, "Local Ca2+ detection and modulation of synaptic release by astrocytes," *Nature Neuroscience*, vol. 14, pp. 1276–1284, Oct. 2011.

[7] A. Panatier, J. Vallée, M. Haber, K. K. Murai, J.-C. Lacaille, and R. Robitaille, "Astrocytes are endogenous regulators of basal transmission at central synapses," *Cell*, vol. 146, pp. 785–798, Sept. 2011.

[8] J. L. Stobart, K. D. Ferrari, M. J. P. Barrett, C. Glück, M. J. Stobart, M. Zuend, and B. Weber, "Cortical Circuit Activity Evokes Rapid Astrocyte Calcium Signals on a Similar Timescale to Neurons," *Neuron*, vol. 98, pp. 726–735.e4, May 2018.

[9] R. Srinivasan, B. S. Huang, S. Venugopal, A. D. Johnston, H. Chai, H. Zeng, P. Golshani, and B. S. Khakh, "Ca(2+) signaling in astrocytes from Ip3r2(-/-) mice in brain slices and during startle responses in vivo," *Nature Neuroscience*, vol. 18, pp. 708–717, May 2015.

[10] E. Shigetomi, E. A. Bushong, M. D. Haustein, X. Tong, O. Jackson-Weaver, S. Kracun, J. Xu, M. V. Sofroniew, M. H. Ellisman, and B. S. Khakh, "Imaging calcium microdomains within entire astrocyte territories and endfeet with GCaMPs expressed using adeno-associated viruses," *The Journal of General Physiology*, vol. 141, pp. 633–647, May 2013.

[11] M. W. Sherwood, M. Arizono, C. Hisatsune, H. Bannai, E. Ebisui, J. L. Sherwood, A. Panatier, S. H. R. Oliet, and K. Mikoshiba, "Astrocytic IP3Rs: Contribution to Ca2+ signalling and hippocampal LTP," *Glia*, vol. 65, pp. 502–513, Mar. 2017.

[12] Y. Otsu, K. Couchman, D. G. Lyons, M. Collot, A. Agarwal, J.-M. Mallet, F. W. Pfrieger, D. E. Bergles, and S. Charpak, "Calcium dynamics in astrocyte processes during neurovascular coupling," *Nature Neuroscience*, vol. 18, pp. 210–218, Feb. 2015.

[13] B. L. Lind, A. R. Brazhe, S. B. Jessen, F. C. C. Tan, and M. J. Lauritzen, "Rapid stimulus-evoked astrocyte Ca2+ elevations and hemodynamic responses in mouse somatosensory cortex in vivo," *Proceedings of the National Academy of Sciences*, p. 201310065, Nov. 2013.

[14] A. Agarwal, P.-H. Wu, E. G. Hughes, M. Fukaya, M. A. Tischfield, A. J. Langseth, D. Wirtz, and D. E. Bergles, "Transient Opening of the Mitochondrial Permeability Transition Pore Induces Microdomain Calcium Transients in Astrocyte Processes," *Neuron*, vol. 93, pp. 587–605.e7, Feb. 2017.

[15] M. Arizono, V. V. G. K. Inavalli, A. Panatier, T. Pfeiffer, J. Angibaud, F. Levet, M. J. T. T. Veer, J. Stobart, L. Bellocchio, K. Mikoshiba, G. Marsicano, B. Weber, S. H. R. Oliet, and U. V. Nägerl, "Structural basis of astrocytic Ca 2+ signals at tripartite synapses," *Nature Communications*, vol. 11, pp. 1–15, Apr. 2020. Number: 1 Publisher: Nature Publishing Group.

[16] E. A. Bushong, M. E. Martone, Y. Z. Jones, and M. H. Ellisman, "Protoplasmic astrocytes in CA1 stratum radiatum occupy separate anatomical domains," *The Journal of Neuroscience: The Official Journal of the Society for Neuroscience*, vol. 22, pp. 183–192, Jan. 2002.

[17] N. A. Oberheim, X. Wang, S. Goldman, and M. Nedergaard, "Astrocytic complexity distinguishes the human brain," *Trends in Neurosciences*, vol. 29, pp. 547–553, Oct. 2006.

[18] T. Kosaka and K. Hama, "Three-dimensional structure of astrocytes in the rat dentate gyrus," *Journal of Comparative Neurology*, vol. 249, no. 2, pp. 242–260, 1986. _eprint: https://onlinelibrary.wiley.com/doi/pdf/10.1002/cne.902490209.

[19] J. Grosche, V. Matyash, T. Möller, A. Verkhratsky, A. Reichenbach, and H. Kettenmann, "Microdomains for neuron–glia interaction: parallel fiber signaling to Bergmann glial cells," *Nature Neuroscience*, vol. 2, pp. 139–143, Feb. 1999.

[20] A. Denizot, M. Arizono, U. V. Nägerl, H. Soula, and H. Berry, "Simulation of calcium signaling in fine astrocytic processes: Effect of spatial properties on spontaneous activity," *PLOS Computational Biology*, vol. 15, p. e1006795, Aug. 2019.

[21] A. Panatier, M. Arizono, and U. V. Nägerl, "Dissecting tripartite synapses with STED microscopy," *Phil. Trans. R. Soc. B*, vol. 369, p. 20130597, Oct. 2014.

[22] A. Denizot, H. Berry, and S. Venugopal, "Computational Modeling of Intracellular Ca2+ Signals in Astrocytes.," *Encyclopedia of Computational Neuroscience*, p. Submitted, 2019. Submitted.

[23] G. W. De Young and J. Keizer, "A single-pool inositol 1,4,5-trisphosphate-receptor-based model for agonist-stimulated oscillations in Ca2+ concentration.," *Proceedings of the National Academy of Sciences*, vol. 89, pp. 9895–9899, Oct. 1992.

[24] I. Bezprozvanny, J. Watras, and B. E. Ehrlich, "Bell-shaped calcium-response curves of Ins(1,4,5)P3- and calcium-gated channels from endoplasmic reticulum of cerebellum," *Nature*, vol. 351, pp. 751–754, June 1991.

[25] F. Santamaria, S. Wils, E. De Schutter, and G. J. Augustine, "The diffusional properties of dendrites depend on the density of dendritic spines," *The European Journal of Neuroscience*, vol. 34, pp. 561–568, Aug. 2011.

[26] Z. Schuss, A. Singer, and D. Holcman, "The narrow escape problem for diffusion in cellular microdomains," *Proceedings of the National Academy of Sciences*, vol. 104, pp. 16098–16103, Oct. 2007. Publisher: National Academy of Sciences Section: Physical Sciences.

[27] A. Reichenbach, A. Derouiche, and F. Kirchhoff, "Morphology and dynamics of perisynaptic glia," *Brain Research Reviews*, vol. 63, pp. 11–25, May 2010.

[28] M. R. Witcher, S. A. Kirov, and K. M. Harris, "Plasticity of perisynaptic astroglia during synaptogenesis in the mature rat hippocampus," *Glia*, vol. 55, pp. 13–23, Jan. 2007.

[29] C. Cali, M. Agus, K. Kare, D. J. Boges, H. Lehvaslaiho, M. Hadwiger, and P. J. Magistretti, "3D cellular reconstruction of cortical glia and parenchymal morphometric analysis from Serial Block-Face Electron Microscopy of juvenile rat," *Progress in Neurobiology*, p. 101696, Sept. 2019.

[30] T. M. Bartol, D. X. Keller, J. P. Kinney, C. L. Bajaj, K. M. Harris, T. J. Sejnowski, and M. B. Kennedy, "Computational reconstitution of spine calcium transients from individual proteins," *Frontiers in Synaptic Neuroscience*, vol. 7, Oct. 2015.

[31] A. Majewska, E. Brown, J. Ross, and R. Yuste, "Mechanisms of Calcium Decay Kinetics in Hippocampal Spines: Role of Spine Calcium Pumps and Calcium Diffusion through the Spine Neck in Biochemical Compartmentalization," *Journal of Neuroscience*, vol. 20, pp. 1722–1734, Mar. 2000.

[32] R. Yuste, A. Majewska, and K. Holthoff, "From form to function: calcium compartmentalization in dendritic spines," *Nature Neuroscience*, vol. 3, pp. 653–659, July 2000.

[33] J. Noguchi, M. Matsuzaki, G. C. R. Ellis-Davies, and H. Kasai, "Spine-Neck Geometry Determines NMDA Receptor-Dependent Ca2+ Signaling in Dendrites," *Neuron*, vol. 46, pp. 609–622, May 2005.

[34] J. Tønnesen, G. Katona, B. Rózsa, and U. V. Nägerl, "Spine neck plasticity regulates compartmentalization of synapses," *Nature Neuroscience*, vol. 17, pp. 678–685, May 2014. Number: 5 Publisher: Nature Publishing Group.

[35] H. Schmidt and J. Eilers, "Spine neck geometry determines spino-dendritic cross-talk in the presence of mobile endogenous calcium binding proteins," *Journal of Computational Neuroscience*, vol. 27, pp. 229–243, Oct. 2009.

[36] A. Biess, E. Korkotian, and D. Holcman, "Diffusion in a dendritic spine: The role of geometry," *Physical Review E*, vol. 76, p. 021922, Aug. 2007. Publisher: American Physical Society.

[37] C. M. Simon, I. Hepburn, W. Chen, and E. D. Schutter, "The role of dendritic spine morphology in the compartmentalization and delivery of surface receptors," *Journal of Computational Neuroscience*, vol. 36, pp. 483–497, June 2014.

[38] M. Bell, T. Bartol, T. Sejnowski, and P. Rangamani, "Dendritic spine geometry and spine apparatus organization govern the spatiotemporal dynamics of calcium," *The Journal of General Physiology*, vol. 151, pp. 1017–1034, Aug. 2019.

[39] D. Holcman and Z. Schuss, "Modeling Calcium Dynamics in Dendritic Spines," *SIAM Journal on Applied Mathematics*, vol. 65, pp. 1006–1026, Jan. 2005.

[40] D. Holcman and Z. Schuss, "Diffusion laws in dendritic spines," *The Journal of Mathematical Neuroscience*, vol. 1, p. 10, Oct. 2011.

[41] A. Cugno, T. M. Bartol, T. J. Sejnowski, R. Iyengar, and P. Rangamani, "Geometric principles of second messenger dynamics in dendritic spines," *Scientific Reports*, vol. 9, pp. 1–18, Aug. 2019. Number: 1 Publisher: Nature Publishing Group.

[42] R. Araya, T. P. Vogels, and R. Yuste, "Activity-dependent dendritic spine neck changes are correlated with synaptic strength," *Proceedings of the National Academy of Sciences*, vol. 111, pp. E2895–E2904, July 2014. Publisher: National Academy of Sciences Section: PNAS Plus.

[43] K. Kucharz, T. Wieloch, and H. Toresson, "Fission and Fusion of the Neuronal Endoplasmic Reticulum," *Translational Stroke Research*, vol. 4, pp. 652–662, Dec. 2013.

[44] N. Holbro, A. Grunditz, and T. G. Oertner, "Differential distribution of endoplasmic reticulum controls metabotropic signaling and plasticity at hippocampal synapses," *Proceedings of the National Academy of Sciences*, vol. 106, pp. 15055–15060, Sept. 2009. Publisher: National Academy of Sciences Section: Biological Sciences.

[45] A. M. B. Reeves, E. Shigetomi, and B. S. Khakh, "Bulk Loading of Calcium Indicator Dyes to Study Astrocyte Physiology: Key Limitations and Improvements Using Morphological Maps," *Journal of Neuroscience*, vol. 31, pp. 9353–9358, June 2011. Publisher: Society for Neuroscience Section: Brief Communications.

[46] W. J. Nett, S. H. Oloff, and K. D. McCarthy, "Hippocampal Astrocytes In Situ Exhibit Calcium Oscillations That Occur Independent of Neuronal Activity," *Journal of Neurophysiology*, vol. 87, pp. 528–537, Jan. 2002.

[47] M. Paukert, A. Agarwal, J. Cha, V. A. Doze, J. U. Kang, and D. E. Bergles, "Norepinephrine controls astroglial responsiveness to local circuit activity," *Neuron*, vol. 82, pp. 1263–1270, June 2014.

[48] A. Skupin, H. Kettenmann, U. Winkler, M. Wartenberg, H. Sauer, S. C. Tovey, C. W. Taylor, and M. Falcke, "How Does Intracellular Ca2+ Oscillate: By Chance or by the Clock?," *Biophysical Journal*, vol. 94, pp. 2404–2411, Mar. 2008.

[49] S. Rüdiger, C. Nagaiah, G. Warnecke, and J. Shuai, "Calcium Domains around Single and Clustered IP3 Receptors and Their Modulation by Buffers," *Biophysical Journal*, vol. 99, pp. 3–12, July 2010.

[50] E. Shigetomi, S. Patel, and B. S. Khakh, "Probing the Complexities of Astrocyte Calcium Signaling," *Trends in Cell Biology*, vol. 26, pp. 300–312, Apr. 2016.

[51] I. Hepburn, W. Chen, S. Wils, and E. De Schutter, "STEPS: efficient simulation of stochastic reaction–diffusion models in realistic morphologies," *BMC Systems Biology*, vol. 6, no. 1, p. 36, 2012.

[52] D. T. Gillespie, "Exact stochastic simulation of coupled chemical reactions," *The Journal of Physical Chemistry*, vol. 81, pp. 2340–2361, Dec. 1977.

[53] S. A. Isaacson and D. Isaacson, "The Reaction-Diffusion Master Equation, Diffusion Limited Reactions, and Singular Potentials," *Physical Review. E, Statistical, Nonlinear, and Soft Matter Physics*, vol. 80, p. 066106, Dec. 2009.

[54] S. Smith and R. Grima, "Spatial Stochastic Intracellular Kinetics: A Review of Modelling Approaches," *Bulletin of Mathematical Biology*, May 2018.

[55] J. Spacek and K. M. Harris, "Three-Dimensional Organization of Smooth Endoplasmic Reticulum in Hippocampal CA1 Dendrites and Dendritic Spines of the Immature and Mature Rat," *Journal of Neuroscience*, vol. 17, pp. 190–203, Jan. 1997.

[56] R. A. McDougal, T. M. Morse, T. Carnevale, L. Marenco, R. Wang, M. Migliore, P. L. Miller, G. M. Shepherd, and M. L. Hines, "Twenty years of ModelDB and beyond: building essential modeling tools for the future of neuroscience," *Journal of Computational Neuroscience*, vol. 42, pp. 1–10, Feb. 2017.

Competing Interests statement

The authors declare no competing financial interests.